Structural, electronic, optical and thermodynamic properties of AlAuO$_2$ and AlAu$_{094}$Fe$_{006}$O$_2$ compounds scrutinized by density functional theory (DFT)

Md. Zuel Rana [a,*], Md. Rajib Munshi [a,b,**], Md. Al Masud [c], Md. Sarwar Zahan [a]

[a] *Department of Physics, European University of Bangladesh, Dhaka, 1216, Bangladesh*
[b] *Nanotechnology Research Laboratory, Department of Physics, Bangladesh University of Engineering and Technology, Dhaka 1000, Bangladesh*
[c] *Department of Industrial and Production Engineering, European University of Bangladesh, Dhaka-1216, Bangladesh*

ABSTRACT

In this study, density functional theory (DFT) simulations have been used to study the structural, electrical and optical properties of AlAuO$_2$ and AlAu$_{094}$Fe$_{006}$O$_2$. Initially, the estimated bandgap of AlAuO$_2$ 0.45, 0.486, 0.419 and 2.49 eV in Perdew-Burke-Ernzerhof (PBE), Revised Perdew-Burke-Ernzerhof (RPBE), PBE for solids (PBE sol) and Becke three-parameter Lee-Yang-Parr (B3LYP) method respectively while AlAu$_{094}$Fe$_{006}$O$_2$ has a zero-band gap after 6 % Fe doping. Then, density of state (DOS) and partial density of state (PDOS) were studied to determine the characteristics of the various orbitals of AlAuO$_2$. The bonding characteristics and thermal stability of this crystal are determined by the Mulliken population charge and thermos physical parameters. Band edge of AlAuO$_2$ was calculated which revealed that the AlAuO$_2$ has suitable oxidation and reduction potential to degrade the contamination. A remarkable absorption has recorded for both AlAuO$_2$ and AlAu$_{094}$Fe$_{006}$O$_2$ in visible and ultraviolet region and capability to utilize photocatalytic dye degradation and hydrogen production through water splitting.

1. Introduction

In the next decades, the world's major energy supply will finally run out. Ultimately, sources of renewable energy are essential for the survival of the entire globe. Currently, solar radiation-based energy is one of the most appealing forms renewable energies. Due to solar energy's availability and vast potential for harnessing, several methods of exploiting it for commercial, industrial, environmental, and other uses have been studied [1,2]. Over the past year, semiconductor nanoparticles have caught the attention of researchers as potential candidates for application in catalyst, photovoltaic, electronic, optoelectronic, and due to their exceptional optical properties [3–5]. For macroscopic solar cells, optoelectronics and photocatalyst, metal oxides have been studied to function as light absorbers, such as ZnO [6], CuO [7], Fe$_2$O$_3$ [8], TiO$_2$ [9], CaO [10], SrTiO$_3$ [11], MoS$_2$ [12], and MgO [13]. However, a colossal challenge to achieve a higher-efficiency semiconductor at ambient temperature from metals (group two to four in periodic table) owing to the broad variety of acceptable circumstances [14–18]. Within these shortcomings, the atomic radii, the broad band gap, and the pricing are the most crucial factors to consider about when making new semiconductor-based devices, even though they have big effects on how

optoelectronic devices absorb or emit ultraviolet (UV) light [19,20]. Crystals of aluminum oxides are some of the most promising alternatives for translucent electronic parts, chemical compound and gas sensing devices, optoelectronics [21–25] and ultraviolet light emitters with a broad energy gap [26,27]. Because of the numerous shapes of Aluminium oxide crystals and Aluminum-based metallic alloys have been used to implant femtolitre-sized specimen into cells [28] and print moveable columns and geometries of EGaIn [29], scientists have been asked to study and develop novel materials with favorable thermochemical properties [30]. In this study, a new material called $AlAuO_2$, which is an alloy of aluminum oxide and gold, has been designed to study its electronic structure, structural configuration, and optical characteristics. The selection of aluminum and gold as the main components was driven by the moderate atomic sizes, resulting in more facile electronic migrations from valence band to conduction band. This results in the creation of many free electrons, which are important for the material's conductivity. The presence of oxygen in $AlAuO_2$ also contributes to the creation of free electrons, Oxygen generates a higher quantity of free electrons compared to aluminum and gold. Consequently, $AlAuO_2$ has been characterized as an n-type material, which means it has more electrons than holes and is a good carrier of electrons. Based on these findings, $AlAuO_2$ has potential applications in a range of electronic devices, including nano sensors, light emitting diodes (LEDs), lasers, and solar cells. This is because it has favorable electronic properties, such as high conductivity and a large number of free electrons, which are important for the functioning of these devices. In order to improve the current conduction of the $AlAuO_2$ material, it was doped with 6 % Fe ($AlAu_{094}Fe_{006}O_2$). The addition of Fe was chosen because it is expected to reduce resistance to flow of electron, leading to improved efficiency. However, there is no limited theoretical and computational studies on $AlAuO_2$, there is an opportunity to investigate the crystal further using Density Functional Theory (DFT) computational simulations. Researchers have employed a first-principles method to investigate various characteristics of the metal oxides crystal, including their electrical structure, structural geometry, thermodynamic properties, and its optical properties. In essence, the purpose of this study was to better understand the properties of the $AlAuO_2$ crystal, and to determine if it can be improved through doping with Fe.

Generalized gradient approximation (GGA) functionals include density and gradient at a specified position. This approach corrects the LDA's overestimation of binding energy in molecules and solids. This allows a more complete description of systems (within limits) and can help characterize certain systems. In large systems where higher-level approaches are impracticable, the Generalized Gradient Approximation (GGA) is commonly used in research. On the other hand, B3LYP hybrid functional was invented in the late 1980s. B3LYP is popular for several reasons. This method was an early development in Density Functional Theory (DFT), which outperformed Hartree-Fock. The B3LYP method outperforms numerous Post Hartree-Fock methods in computational performance while yielding comparable results. When applied to the DFT, this method is quite robust. Hybrid functionals improve the accuracy of properties that strongly depend on a material's energy spectrum, like defect energy levels in a semiconductor's bandgap. By using DFT, our aim is to provide a detailed understanding of the crystal's structure, electronic properties, and other relevant characteristics, which will help to inform future studies and applications of this material. Doping is a process in which impurities are introduced into a material to modify its properties. In this study, Fe incorporation impact of $AlAuO_2$ was examined comprehensively for the first time. The aim is to
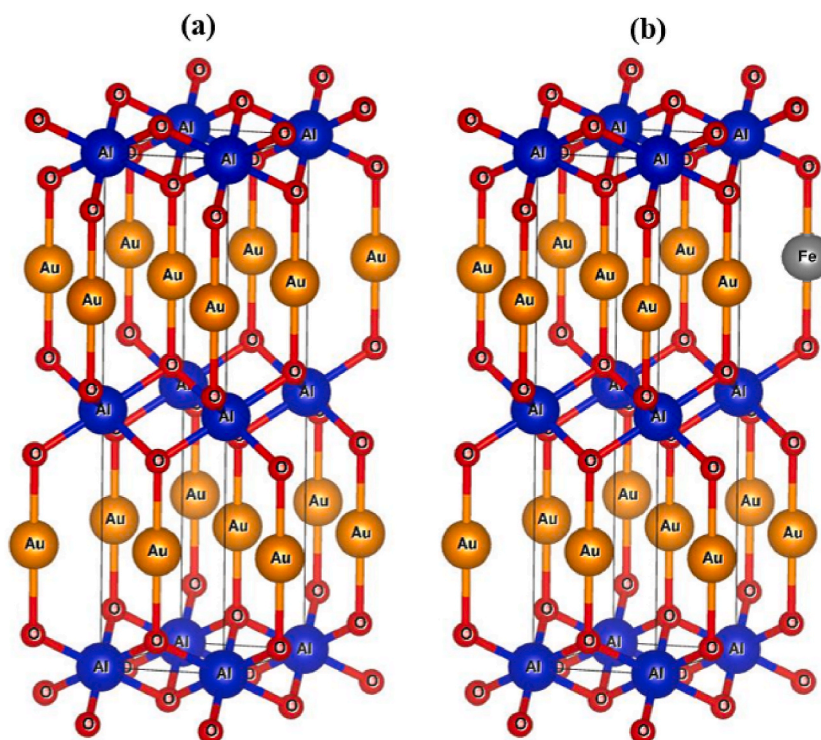

Fig. 1. (a) Structures of $AlAuO_2$ and (b) Structures of $AlAu_{094}Fe_{006}O_2$ (gray sphere is Fe atom) respectively.

understand how the doping process can be used to modify the material's structural, electrical, and optical properties. To obtain accurate results, three different computational simulation methods were used such as GGA with PBE, RPBE, and PBESol functionals and also, a hybrid method used named Becke three-parameter Lee-Yang-Parr (B3LYP). These approaches are utilized to conduct a comparative examination of the characteristics of the doped $AlAuO_2$ crystal in order to get a more precise knowledge of the impacts of the doping process.

2. Computational method

In this study, generalized gradient approximation (GGA) with Perdew-Burke-Ernzerhof (PBE) method has been employed to calculate various properties of $AlAuO_2$ and Fe atom-doped $AlAuO_2$ crystal. The calculations were carried out by utilizing Cambridge Sequential Total Energy Package (CASTEP) based on the DFT and the results obtained were considered to be the most reliable and acceptable. A cut-off energy of 550 eV and a k-point of $4 \times 4 \times 1$ was used in conjunction with norm-conserving pseudopotentials in order to determine the bandgap, total and partial density of state (DOS, PDOS) respectively. Additionally, optical attributes were performed to determine the reflective properties, absorption coefficient, index of refraction, dielectric property, conductivity of the material, and the loss function. Before energy calculation, geometric optimization was carried out and the consolidation requirement for force among the atoms was set at 3×10^{-6} eV/Å. The elastic limit was set at 1×10^{-3} Å while the maximum energy and stress were set at 1×10^{-5} eV/atom and 5×10^{-2} GPa, respectively [31]. The Fe element was doped into the $AlAuO_2$ crystal structure by replacing Au atoms with a doping ratio of 6 %. This doping ratio was optimized as the minimum portion of doping while still maintaining the symmetry pattern of the crystal structure.

3. Results and discussions

3.1. Optimized structure

The crystalline structure of a material has a significant impact on its properties. To understand a material's properties, it is necessary to understand its structure. The calculated structure of $AlAuO_2$ and $AlAu_{094}Fe_{006}O_2$ are depicted in Fig. 1 (a, b). $AlAuO_2$ and $AlAu_{094}Fe_{006}O_2$ are two crystals with an optimized hexagonal structure, which has a lattice constant of 2.886 Å for both a and b, and

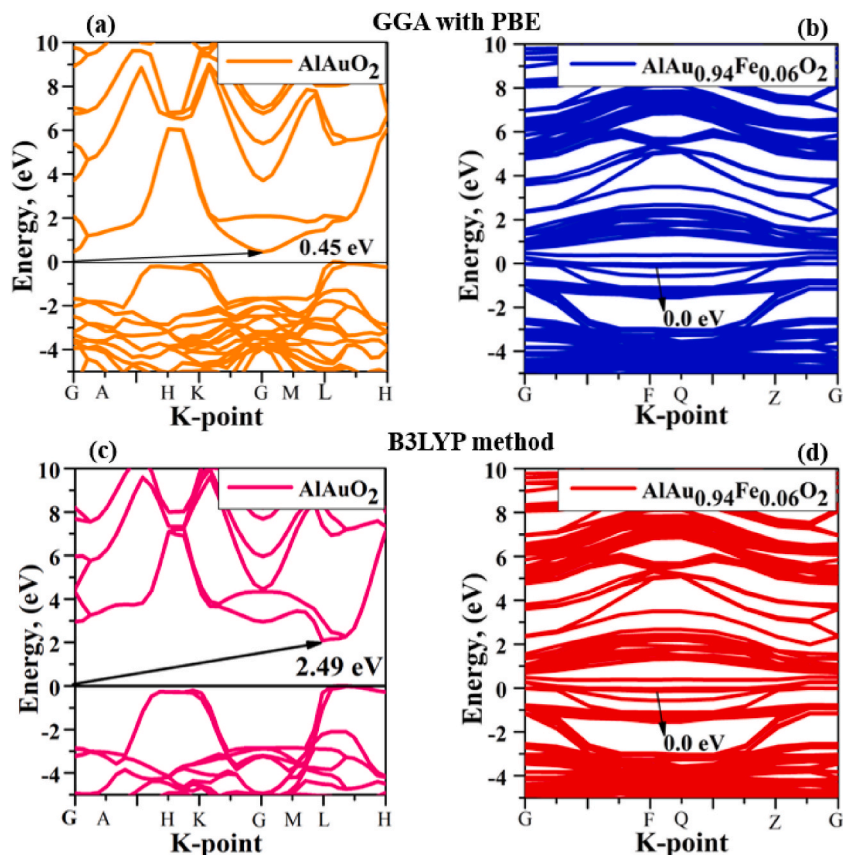**Fig. 2.** Electronic band structure of $AlAuO_2$ and $AlAu_{094}Fe_{006}O_2$ in GGA with PBE (a, b) B3LYP method (c, d) respectively.

12.362 Å for c, having $\alpha = \beta = 90°$ and $\gamma = 120°$. The structure is described as a Hermann-Mauguin symbol of $P6_3/mmc$ and Hall symbol of P6c/2c [32].

In the case of $AlAuO_2$, as shown in Fig. 1(a), the cations Al^{3+} and Au^+ are positioned at four apex angles of a tetrahedral structure, whereas the anion O^{2-} is placed in the middle. Au^+ is bonded with two identical O^{2-} atoms in geometry, and Al^{3+} is bonded to six identical O^{2-} atoms, forming an edge-sharing AlO_6 octahedron, resulting in Au–O and Al–O chemical bonds. Similarly, in the case of $AlAu_{094}Fe_{006}O_2$, as shown in Fig. 1(b), the cations Al^{3+}, Au^+, and Fe^{2+} and the anion O^{2-} form various chemical bonds such as Al–O, Au–O, and Fe–O, respectively.

3.2. Electronic band structure

The electronic band structures of two compounds, $AlAuO_2$ and $AlAu_{094}Fe_{006}O_2$, were analyzed using some distinct computational methods: Generalized Gradient Approximation (GGA) with Perdew-Burke-Ernzerhof (PBE) exchange-correlation functional, and a hybrid method Becke three-parameter Lee-Yang-Parr (B3LYP) shown in Fig. 2(a–d). Other two method such as GGA with revised Perdew-Burke-Ernzerhof (RPBE) functional and GGA with PBESol, a revised Perdew-Burke-Ernzerhof are shown in ESI*(Figs. S1 (a–d)).

In this calculation, the zero of energy was defined as the Fermi energy level. By analyzing the electronic band structures of $AlAuO_2$ using the GGA using PBE method and it was found that the conduction bands of this compound had a minimum value at a point located between the K and M symmetry points. On the other hand, the height value of valence bands was found at the K symmetry point. As a result of this band structure, the band gap of $AlAuO_2$ was determined to be indirect, with a magnitude of 0.45 eV.

The introduction of Fe impurities into $AlAuO_2$ at a concentration of 6 % caused a significant alteration in the electrical band structure of desired material. This resulted by zero band gap as determined by the GGA with PBE method. Table 1 shows the band gap values obtained from three different computational methods for $AlAuO_2$ and $AlAu_{094}Fe_{006}O_2$.

Specifically, the GGA with RPBE approach resulted in an indirect band gap of 0.486 eV for $AlAuO_2$ and a direct band gap of 0.00 eV for $AlAu_{094}Fe_{006}O_2$. Similarly, GGA with PBESol method generated values of 0.419 eV and zero for the band gaps of $AlAuO_2$ and $AlAu_{094}Fe_{006}O_2$, respectively. It is noteworthy that all three methods yielded similar results for the band gaps of these compounds. Another hybrid was performed method B3LYP, which provided the value of band gap 2.49 eV and 0.00 eV for $AlAuO_2$ and $AlAu_{094}Fe_{006}O_2$, respectively. The bonding properties of $AlAuO_2$ and $AlAu_{094}Fe_{006}O_2$ crystals have been studied by analyzing their Mulliken atomic populations [33,34].

This analysis helps to understand how different types of atoms in a substance overlap and share charges. Both materials consist of positively and negatively charged atoms, with Al, Au, and Fe having positive charges and oxygen having negative charges. The observed atomic charges of these elements in $AlAuO_2$ and $AlAu_{094}Fe_{006}O_2$ are presented in Table 2. These results indicate that charge is transferred from the Al, Au, and Fe atoms to the oxygen atom, which acts as a charge receptor.

3.3. States of total and partial density

To understand the character of energy band structures and the dispersion of orbitals in crystal of $AlAuO_2$ and $AlAu_{094}Fe_{006}O_2$, the density of states (DOS) and partial density of states (PDOS) of Al, Au, Fe, and O elements were determined using the GGA with PBE method [35]. The results showed that $AlAu_{094}Fe_{006}O_2$ had a higher electron density in the valence band compared to $AlAuO_2$, as shown in Fig. 3(a–b). The analysis of the electron transition resulting from hybridization in $AlAuO_2$ was conducted through the study of the partial density of states (PDOS) presented in Fig. 3(c and d). By examining the PDOS, it was discovered that the dominant peak in the band of conduction originated from the collaborative influence of the p-orbital at approximately 2 eV and the s-orbital at 7.5 eV. The p-orbital in the conduction band had the highest contribution and the d-orbital had the same as p orbital contribution in the valence band of $AlAuO_2$. The electronic structure of a $AlAuO_2$ is such that the valence band is primarily made up with p and d orbitals, while the conduction band is formed from a combination of different orbitals. Specifically, the conduction band is made up of the $3p^1$ orbital of aluminum (Al), the $5d^{10}$ and $6s^1$ orbitals of gold (Au), and the $2p^4$ orbital of oxygen (O).

In the case of $AlAu_{094}Fe_{006}O_2$, the PDOS consisted of the $3s^2$ and $3p^1$ orbitals of Al, the $5d^{10}$, $5p^6$ and $6s^1$ orbitals of Au, the $3d^6$ and $4s^2$ orbitals of Fe, and the $2s^2$ and $2p^4$ orbitals of O. The conduction band in the Fe atom was primarily influenced by the p-orbital, which had the highest contribution within the energy range of 0–2.5 eV. Additionally, the d and s orbitals also had an impact on the conduction band, with contributions occurring at energies of 1 and 2.5 eV, respectively. In contrast, the valence band of the Fe atom was influenced by the d and p orbitals, which had the highest contributions at energies of 2.5 and 4 eV, respectively. $AlAu_{0.94}Fe_{0.06}O_2$ showed the highest contribution from the d-orbital inside conduction band, and the incorporation of Fe dropped the energy band gap energy to 0.00 eV. The contribution of s, p and d orbitals in $AlAuO_2$ and $AlAu_{094}Fe_{006}O_2$was further compared and is shown in ESI*

Table 1
The values of band gap of $AlAuO_2$ and $AlAu_{094}Fe_{006}O_2$ through different methods.

Samples name	Bandgap			
	GGA with PBE	GGA with RPBE	GGA with PBESol	B3LYP
$AlAuO_2$	0.45 eV	0.48 eV	0.41 eV	2.49 eV
$AlAu_{0.94} Fe_{0.06} O_2$	0.00 eV	0.00 eV	0.00 eV	0.00 eV

Table 2
The values of charge population, bond length, and Hirsfeld charge in GGA with PBE method of AlAuO$_2$ and AlAu$_{094}$Fe$_{006}$O$_2$.

Compound Name	Element	Charge (e)	Bonding element	Population	Bond length (Å)	Hirsfield charge (e)
AlAuO$_2$	Al	1.60	Al–O	0.99	1.88310	0.36
	Au	0.24	Au–O	0.13	2.18467	0.26
	O	−0.92	O–O	−0.32	2.45342	−0.31
AlAu$_{094}$Fe$_{006}$O$_2$	Al	1.64	Al–O	0.35	1.83052	0.37
	Au	0.19	Au–O	0.32	1.98271	0.23
	Fe	0.25	Fe–O	0.42	1.83183	−0.03
	O	−0.94	O–O	−0.15	1.98271	−0.30
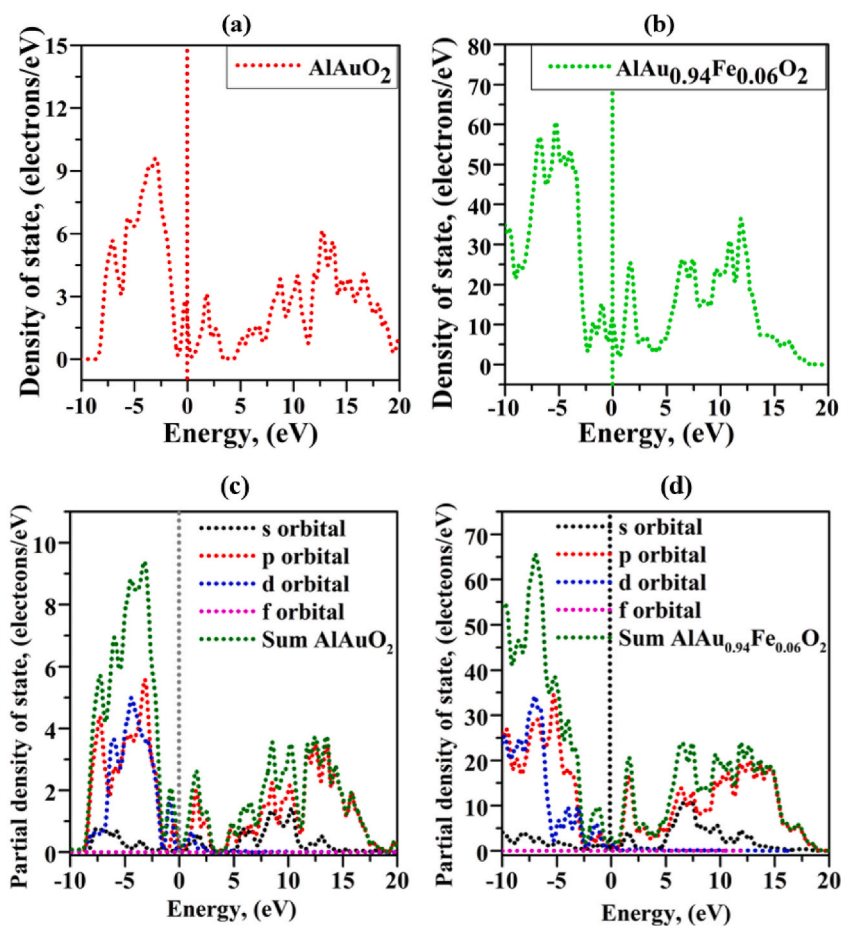
Fig. 3. (a, b) States of density and (c, d) partial density of state of AlAuO$_2$ and AlAu$_{094}$Fe$_{006}$O$_2$ in GGA with PBE method.

(Figs. S2(a–g)). It was found that the contribution of s and p orbitals was almost the same in both AlAuO$_2$ and AlAu$_{094}$Fe$_{006}$O$_2$, while d-orbital contributed differently. The d-orbital had the highest contribution in the conduction band within the zone of 0.0–2.5 eV in AlAu$_{094}$Fe$_{006}$O$_2$, while both p and s orbitals had a contribution in both AlAuO$_2$ and AlAu$_{094}$Fe$_{006}$O$_2$ after 1.0 eV.

3.4. Optical properties

The optical characteristics of a solid are crucial for the investigation of its band structure, resonances, impurity levels, localized flaws, and lattice vibrations. To study of optical characteristics of both AlAuO$_2$ and Fe-doped AlAu$_{094}$Fe$_{006}$O$_2$ crystals, some studies have been conducted to measure their absorbance, reflectivity, index of refraction, dielectric function, dielectric loss function and conductivity. Optical properties of AlAuO$_2$ and AlAu$_{094}$Fe$_{006}$O$_2$ were analyzed to understand how the introduction of Fe atoms affects these properties to predict the photovoltaic, optoelectronic and photocatalytic properties.

3.4.1. Optical reflectivity

In recent years, there has been an increase in interest in the production of regularly spaced vacancy layers inside the postmodern phase of Al–Au–O_2-based materials. This is due to the fact that these electron delocalization processes promote a transition from insulator to metal. It is essential, in order to investigate the potential of this vacancy regulating phenomenon, to construct the crystalline structure of the postmodern phase in a manner that is distinct from the strongly linked thermally stable phase. The optical characterizations of solids play an important role in investigating band structure, resonances, impurity levels, localized flaws, and vibrations of lattice. There is a one-to-one correspondence between the structure of energy bands of solids and either the dielectric function or the complex conductivity. The absorbance, reflectivity, index of refraction, dielectric function, dielectric loss function and conductivity. Optical properties of $AlAuO_2$ and $AlAu_{094}Fe_{006}O_2$ have analyzed. Reflectivity is a key tool in analyzing the optoelectronic and photovoltaic behaviors of $AlAuO_2$ and $AlAu_{094}Fe_{006}O_2$, as it is directly related to the absorbance capability of the material and the transfer of electrons from the valence band towards the conduction band. It has been reported that a lower reflectivity indicates a greater absorption of visible or ultraviolet radiation.

Fig. 4(a) demonstrated that the reflectivity of $AlAuO_2$ and $AlAu_{094}Fe_{006}O_2$ begins at 0.68 and 0.29, from the starting frequency respectively. For $AlAuO_2$, the reflectivity has a lower value until 1.75 eV and then reached to height value of 0.66 at 1.75 eV. In the case of $AlAu_{094}Fe_{006}O_2$, the reflectance shifts in vigorously, but it is somewhat smaller than that of AlAuO2. The value of reflectance is much lower than the value of absorption for the both $AlAuO_2$ and $AlAu_{094}Fe_{006}O_2$.

3.4.2. Conductivity

The electronic conductance of semiconductors is related to the distribution of electrons in orbitals and energy bands. In a crystal lattice, conduction can occur when there are free electrons and holes present. The conductivity of $AlAuO_2$ and $AlAu_{094}Fe_{006}O_2$ depicted in Fig. 4(b) The conductivity of the doped material $AlAu_{094}Fe_{006}O_2$ was found to be slightly greater than the pure $AlAuO_2$. The real parts of the conductivity increased gradually from 1.75 eV until 2.75 eV and then increased rapidly, while the imaginary parts decreased little change at the end in the opposite direction. The conductivity's top peak was found to reach about 10 1/fs at 3.0 eV for $AlAu_{094}Fe_{006}O_2$. The results of the study showed that conductivity increased after 6 % Fe doping.

3.4.3. Loss function

The energy loss function (ELF) is a fundamental physical quantity describing the interaction between electrons and matter in solids and is essential for quantitative evaluation of inelastic scattering during electron transport in solids.

In contrast, the low energy region, below 3.0 eV according to Fig. 5(a), gives more information on the sample's composition and electrical structure. The loss function of $AlAu_{094}Fe_{006}O_2$ is seen to be higher than $AlAuO_2$ in the low energy region, indicating the much more loss of energy due to the electrical structure and composition elements in the sample. However, there is a significant change of loss function in between $AlAuO_2$ and $AlAu_{094}Fe_{006}O_2$, suggesting that there is significant difference in the d-orbital splitting between the two samples.

3.4.4. Dielectric function

To understand the optical properties of materials, dielectric function is a crucial tool which are closely tied to the adsorption properties of solids. It is defined as:

$$(\omega) = \varepsilon_1(\omega) + i\varepsilon_2(\omega) \tag{1}$$

In equation [1] $\varepsilon_1(\omega)$ is the dielectric constant (the real part) whereas $\varepsilon_2(\omega)$ is the dielectric loss factor (the imaginary part), respectively. The dielectric function, which is connected with absolute permittivity or permittivity and characterizes the material space. The
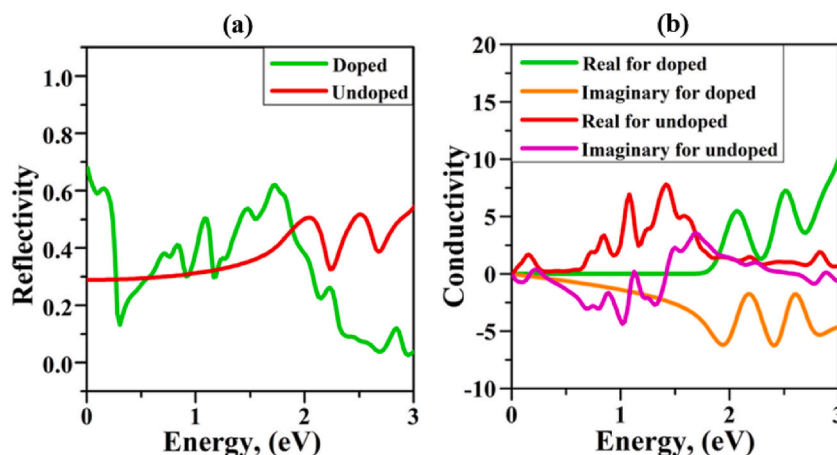

Fig. 4. (a) Optical reflectivity and (b) Optical conductivity of $AlAuO_2$ and $AlAu_{094}Fe_{006}O_2$ in PBE method.
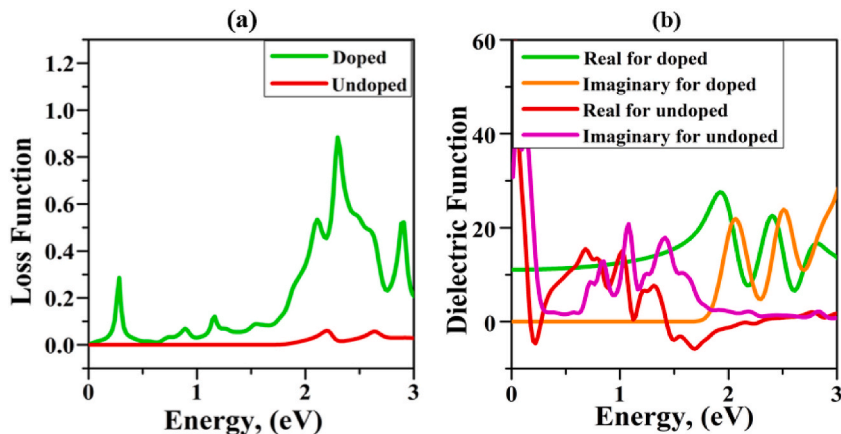
Fig. 5. (a) Optical Loss function (b) Dielectric function of $AlAuO_2$ and $AlAu_{094}Fe_{006}O_2$ in GGA with PBE method.

dielectric function's real part represents the energy storage capability of the solid material when it is placed in electric field, whereas dissipation capacity is indicated by the imaginary part. As seen in Fig. 5 (b), for the both materials, the real parts exhibit greater value, making them suitable for use as electrostatic cell materials for energy storage. Furthermore, $AlAu_{094}Fe_{006}O_2$ is shown to be a more effective material than $AlAuO_2$ for use as an electrostatic cell.

3.4.5. Index of refraction

The refractive index of a substance quantifies the relative change between the velocity of light in that medium and in a vacuum. A higher refractive index indicates a denser medium which can gives low absorption. The refractive index of $AlAuO_2$ and $AlAu_{094}Fe_{006}O_2$ which is an attribute of the photon energy and consists with real and imaginary part depicted in Fig. 6 (a, b). For optoelectronic applications, a higher value of the real part of the index of refractive is desirable, while the opposite is true for the imaginary part. At low photon energies, both $AlAuO_2$ and $AlAu_{094}Fe_{006}O_2$ have a high real part of the refractive index and $AlAuO_2$ has a near-zero imaginary part. The real and imaginary component of refractive index remains stable before 1.5 eV, after that it is vigorously increasing with the increasing photon energy for $AlAuO_2$. It is noted that, the real part of $AlAu_{094}Fe_{006}O_2$ is lower than $AlAuO_2$ after 1.1 eV photon energy, which making it a better material for use in the desired area, despite its band gap being around 0.45 eV.

3.4.6. Optical absorption

The optical absorbance of $AlAuO_2$ and $AlAu_{094}Fe_{006}O_2$ materials was analyzed by utilizing the polycrystalline polarization method and applying a small smearing value of 0.1 to clearly distinguish the absorption peaks. Fig. 7 illustrates the findings, which represent the absorption as a function of the photon energy. The absorbance peaks indicate the occurrence of transfer of electron from maximum valence band (MVB) to maximum conduction band (MCB) due to the incident light, particularly in the visible range.

The absorbance for $AlAuO_2$ is observed that it is increased randomly from 0.0 to 4 eV and then sharply increased after 4 eV. On the other hand, the Fe-doped crystal ($AlAu_{094}Fe_{006}O_2$) shows higher absorption, with more peaks than the undoped crystal. The
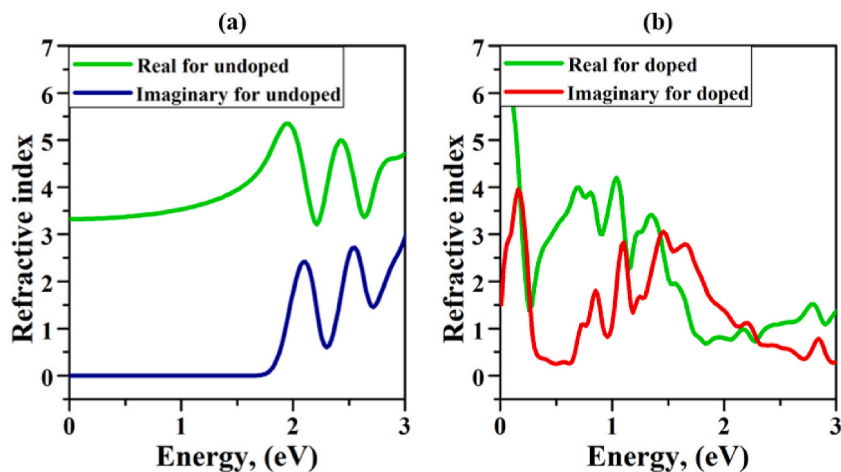

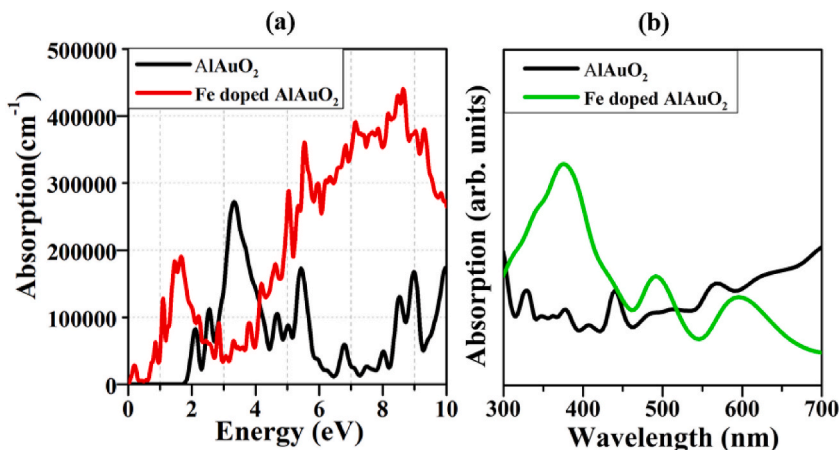**Fig. 6.** Refractive index (a) Real part (b) Imaginary part of $AlAuO_2$ and $AlAu_{094}Fe_{006}O_2$ in GGA with PBE method.

Fig. 7. (a) Optical absorption vs. energy in eV (b) Optical absorption vs. energy in nm of $AlAuO_2$ and $AlAu_{094}Fe_{006}O_2$.

absorbance level of $AlAu_{094}Fe_{006}O_2$ is higher than that of $AlAuO_2$ from 1.0 to 10.0 eV shown in Fig. 7 (a).

The results indicate that the doped material has a narrower energy gap, sometime it will be zero and greater absorbance compared to the pure material. Additionally, the doped material displayed a greater range of photon energy absorption capabilities. Furthermore, Fig. 7 (b), represented the absorption coefficient of $AlAuO_2$ and $AlAu_{094}Fe_{006}O_2$ materials depending on wavelength in the visible light region. The height peak of absorbance was found at about 380 nm, 480 nm and 600 nm for $AlAu_{094}Fe_{006}O_2$ crystal while the maximum peak of absorption for $AlAuO_2$ was obtained at 330 nm, 440 nm respectively. Therefore, these materials might be highly adept at utilizing the visible and ultraviolet energy regions. However, $AlAu_{094}Fe_{006}O_2$ crystal exhibit more promising absorbance compared to $AlAuO_2$ in visible and ultraviolet region. These properties make the doped material a suitable candidate for use in various optical
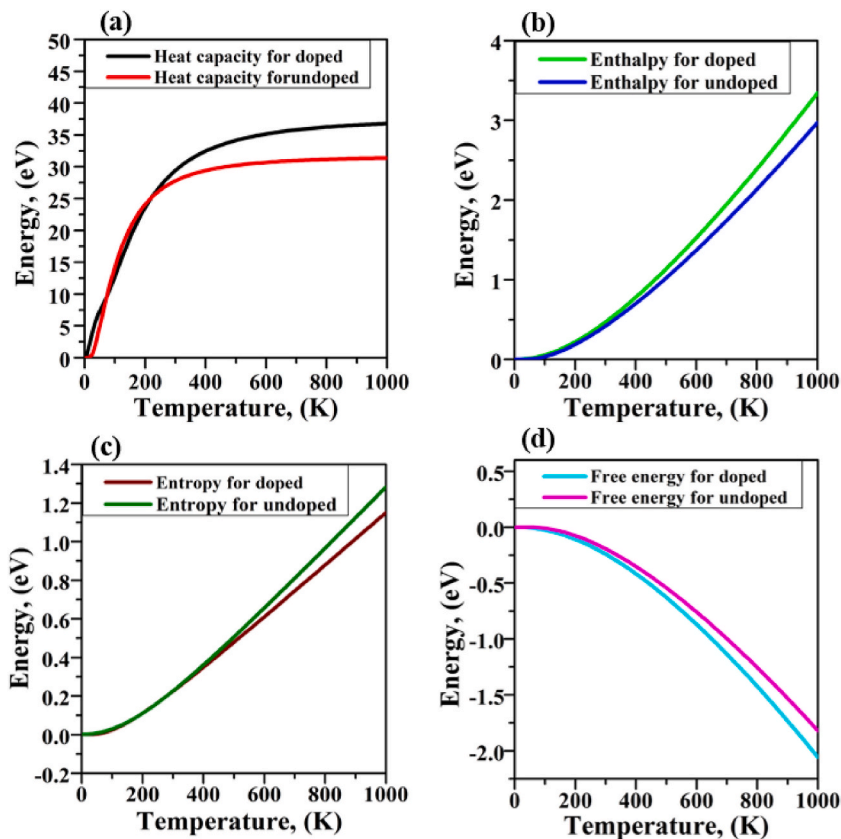

Fig. 8. Thermodynamic properties of $AlAuO_2$ and $AlAu_{094}Fe_{006}O_2$ (a) Heat capacity (b) Enthalpy (c) Entropy (d) Free energy in GGA with PBE method.

communication devices and in the construction of additional transoms, skylights, and window planes for semiconducting materials in the field of optoelectronic devices [36,37].

3.5. Thermoelectric properties

Thermodynamic qualities describe a system's energy content. A system in thermal equilibrium has measurable thermodynamic properties. Most thermodynamic parameters include enthalpy, entropy, Gibbs free energy, and internal energy. Enthalpy represents a system's heat content under constant pressure. Entropy measures system dysfunction. Gibbs free energy measures a system's work capability, while internal energy includes all its energy. Dedicated equipment is needed to quantify these properties. Thermodynamic features help create new systems and predict system dynamics. Thermoelectric properties arise from the interaction between heat and electronic transportation in chemical and physical processes, and define the ability of a material to generate an electric potential in response to a temperature difference or vice versa, the transfer of energy during biochemical reactions and the connection between a given system and its external and internal environments [38–40]. Thermodynamics includes numerous essential concepts, such as enthalpy, heat capacity, free energy and entropy, which are most important in understanding the behavior of physical systems. These ideas are important to both physics and physical chemistry, and they offer a framework for understanding and predicting the behavior of many different systems. According to Petersen et al. there is a close relationship between entropy and enthalpy in thermodynamics. These concepts are related by the Gibbs free energy equation, which describes how changes in a system's entropy and enthalpy relate to changes in its free energy. Entropy, which measures the degree of disorder in a system, can be a useful indicator of the discharge condition of a substance. This is because changes in entropy can reflect changes in the configuration and organization of the substance's molecules during a discharge process, providing important information about the substance's behavior and state.

3.5.1. Heat capacity

The quantity of energy that is required to get the temperature of a substance up to a certain level is referred to as heat capacity of a substance. This quantity of energy is the maximum amount of heat the thing can hold. Temperature is a measurement of the overall average kinetic energy of the particles that make up a material. Heat transfers heat energy from hotter regions to colder region. The total number of degrees of freedom of constituent particles is utilize to measure heat capacity of a thermodynamical system. The greater the number of degrees of freedom represent the more energy the system can store, and system has higher heat capacity. These degrees of freedom can include translational, rotational, and vibrational motions of the particles, and they all contribute to the system's overall ability to absorb and release heat [41]. Fig. 8 (a) displays the results of a study that compared the total heat capacities of $AlAuO_2$ and $AlAu_{094}Fe_{006}O_2$. $AlAu_{0.94}Fe_{0.06}O_2$ crystals have a higher heat capacity than $AlAuO_2$ crystals, yet both exhibit the same degree of variability in this regard. Maximum heat capacities of $AlAu_{094}Fe_{006}O_2$ and $AlAuO_2$ at 1000 K are 35 eV and 30 eV, respectively. This material is suitable for use in the field optoelectronic devices because it has a much higher heat capacity.

3.5.2. Enthalpy

Enthalpy is a unit of energy measurement in thermodynamics. It indicates a system's total heat energy, determined by the summation of the internal energy with the pressure-volume product. Enthalpy is the technical name for the amount of energy needed to build a structure and make room for it by setting its pressure, volume, and displacement. The idea of enthalpy includes the highest non-mechanical activity and the highest possible temperature of the exhaust. Enthalpy is a crucial factor in any productive work, as it involves the measurement of heat or temperature contained within a body [42]. The following mathematical equations [2,3] are employed to define enthalpy.

$$H = U + PV \tag{2}$$

$$dH = TdS + PdV \tag{3}$$

Enthalpy is represented by the letters H, internal energy is expressed by U, P for pressure, and V for volume, respectively. The enthalpy of $AlAuO_2$ and $AlAu_{094}Fe_{006}O_2$ increases from 100 to 1000 K and maximum at 1000 K as shown in Fig. 8 (b). However, $AlAu_{094}Fe_{006}O_2$ show more significant value of enthalpy than $AlAuO_2$.

3.5.3. Entropy

Entropy is a measurement of the amount of randomness or dispersion in the energy of the components, such as atoms or molecules, in a system. As entropy rises, the energy is spread more uniformly and the system becomes less structured and more chaotic [43]. Additionally, it is a distinctive characteristic of thermal systems that varies in relation to the quantity of matter, and it is used to measure the degree of order of the system. This fundamental property of thermodynamic systems means that value changes depending on the amount of material present. Entropy may have a positive or negative value. In accordance with the second law of thermodynamics, the entropy of a system may only reduce if the entropy of another system increases. Fig. 8 (c) represented the entropy of $AlAuO_2$ and $AlAu_{094}Fe_{006}O_2$. Among the two materials $AlAuO_2$ has the greater value of entropy than $AlAu_{094}Fe_{006}O_2$. As seen in Fig. 8 (c), when the temperature rises, the entropy of both materials increases.

3.5.4. Free energy

This term usually refers to the amount of energy available to do useful work in a system. Free energy is a thermodynamic potential that is dependent on the system's internal energy and entropy. The free energy of a system can be changed by changing its internal

energy or its entropy. The two essential parameter of free energy include the Helmholtz (F) and Gibbs (G), expressed by equations [4–6] as:

$$F = U - TS \tag{4}$$

$$G = H - TS, \left(Where, H = U + PV \text{ is the enthalpy} \right) \tag{5}$$

$$G = U + PV - TS \tag{6}$$

Where U represent the internal energy, TS indicates that the multiplication of temperature and entropy and PV stands for the combination of pressure and volume. Changes of free energy are used to estimate the work done of a thermal process. It was observed that the permitted energy of $AlAuO_2$ and $AlAu_{094}Fe_{006}O_2$ initiates at 178 K and continuously changes with increasing temperature which is shown in Fig. 8 (d). Fig reveal that $AlAu_{094}Fe_{006}O_2$ has more free energy than $AlAuO_2$ crystal.

3.6. Photocatalytic mechanism

A photo-catalyst required both a high redox potential and robust light absorption capabilities to function well in visible light. The electron transfer to the surface of adsorbates is reliant on both the redox potential and the location of band edges, which must be adequate for the process to occur effectively [44]. The band edge's locations of the samples were estimated by Mulliken electronegativity and the value of band gap of $AlAuO_2$ using B3LYP method, which are shows using the following equations [7,8,45].

$$E_{VB} = X - E_e + \frac{1}{2} E_g \tag{7}$$

$$E_{CB} = E_{VB} - E_g \tag{8}$$

Where, E_{VB} is represented valence edge whereas E_{CB} is for conduction edge potential respectively and Mulliken electronegativity express by χ which stands for the average geometric quantity, E_e the electron's free energy having value near to 4.5 eV through hydrogen scale [46]. The expected band gap value, Eg, was determined using the B3LYP method which is shown in Table 1. Based on our research, the potential of edge the of valence band was determined for $AlAuO_2$ is around 2.41 eV shown in Fig. 9 (a), whereas the potential of conduction band edge is about −0.075 V. The obtained values are shown in Fig. 8 which displayed an illustration of photocatalytic mechanism and the band edge position of $AlAuO_2$. The redox potential of $AlAuO_2$ is determined by band edges positions. A positive valence band maximum (VBM) potential indicates that the material has a high capacity to oxidize, while a negative conduction band minimum (CBM) potential suggests a high potential for reduction by electrons [47]. $AlAuO_2$, as we hypothesized, has strong oxidation capabilities that allow them to generate oxygen from water. This is because the valence band potential of these materials is so high. In the presence of holes or highly oxidizing agents like O^{2-}, H_2O_2, and ·OH, organic pollutants are degraded photocatalytically owing to their greater oxidation capacities. The strong oxidative capability of these materials degrades organic contaminants. $AlAgO_2$ (2.41 V) has greater VBM potentials than E_o (O_2/H_2O) (1.23 eV). These materials oxidize water and produce reactive oxygen species, which break down organic contaminants [48,49]. After that, a portion of the O_2 then interacted with the H^+ to produce H_2O_2, another catalytic molecule. Furthermore, the potential of CVM of $AlAuO_2$ is −0.075 eV, which is greater than E_o (H^+), indicating the capability of $AlAuO_2$ to decrease H^+ by producing H_2 through the water splitting.

The outstanding photocatalytic performance $AlAuO_2$ in breaking down organic contaminants is primarily attributed to its oxidation potential of holes, O^{2-}, and H_2O_2. Hopefully this material will perform significantly in the field of photocatalytic dye degradation as well as photocatalytic hydrogen generation. The band gap of $AlAu_{094}Fe_{006}O_2$ was calculated 0.0 eV so, it is impossible to calculate band edge position for this doped material. For this reason, it is quite difficult to predict the photocatalytic properties of
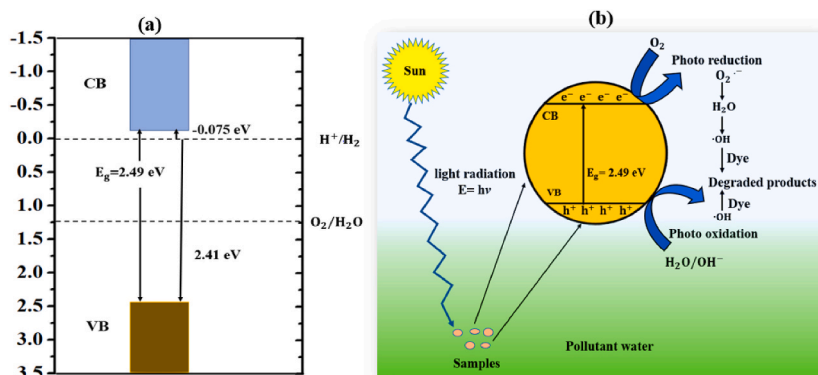

Fig. 9. **(a)** Band edge potential **(b)** Dye degradation mechanism of $AlAuO_2$.

AlAu$_{094}$Fe$_{006}$O$_2$ but the experimental result may be changed. The graphical representation of photocatalytic performance of AlAuO$_2$ depicted in Fig. 9 (b) and the probable reaction can be expressed by equations [9–12] as follows;

$$AlAuO_2 + h\nu \rightarrow AlAuO_2 \ (e^- + h^+) \tag{9}$$

$$AlAgO_2(e^-) + O_2 \rightarrow O^{2-} \tag{10}$$

$$AlAuO_2 \ (h^+) + H_2O \rightarrow H^+ + {}^{\cdot}OH \tag{11}$$

$$Dye(MB, RhB \ etc.) + \left(O^2, OH, e^-, h^+\right) \rightarrow non \ toxic \ byproducts \tag{12}$$

4. Conclusion

The study of the optoelectronic properties of AlAuO$_2$ and AlAu$_{094}$Fe$_{006}$O$_2$ using computational tools revealed that AlAuO$_2$ was discovered as a material with narrower bandgap energy while 6 % Fe doped crystal was considered as a material with zero band gap energy to utilize in optoelectronic devices. The band gap of AlAuO$_2$ was calculated to be 0.45 eV using the PBE method of the GGA functional. Further study with the GGA with RPBE, with GGA with PBESol and B3LYP methods, respectively, resulted in values of 0.486 eV, 0.419 eV and 2.49 eV. The 6 % Fe doping resulted in a decrease in the electronic band gap of AlAu$_{094}$Fe$_{006}$O$_2$ and finally reached to 0.0 eV. The results indicated that AlAu$_{094}$Fe$_{006}$O$_2$ was a better material to utilize in the field of optoelectronic devices than AlAuO$_2$ due to its superior absorption and conductivity. However, AlAu$_{094}$Fe$_{006}$O$_2$ was found to be good thermally and chemically stable than AlAuO$_2$ based on entropy and free energy calculations. Nevertheless, both AlAu$_{094}$Fe$_{006}$O$_2$and AlAuO$_2$ showed perfect crystal behavior at room temperature. Based on this investigation, this material can be utilized in the field of optoelectronic devices and photocatalytic dye degradation as well as hydrogen generation through the water splitting.

Data availability statement

Data included in article/supplementary material/referenced in article.

CRediT authorship contribution statement

Md Zuel Rana: Conceptualization, Data curation, Formal analysis, Investigation, Methodology, Software, Validation, Visualization, Writing – original draft, Writing – review & editing. **Md Rajib Munshi:** Conceptualization, Data curation, Software, Supervision, Formal analysis, Investigation, Methodology, Writing - review & editing. **Md Al Masud:** Data curation, Writing – review & editing. **Md Sarwar Zahan:** Data curation, Writing – review & editing.

Declaration of competing interest

The authors declare that they have no known competing financial interests or personal relationships that could have appeared to influence the work reported in this paper.

We confirm that this work is original and has neither been published elsewhere nor it currently under consideration for publication. All authors of this research paper have actively participated in conceiving the research plan and implementing the theoretical works and analysis. All authors have read and approved the final version of the manuscript being submitted. To the best of our knowledge, no conflict of interest, financial or other, exists.

Appendix A. Supplementary data

Supplementary data to this article can be found online at https://doi.org/10.1016/j.heliyon.2023.e21405.

References

[1] A.M. Tama, S. Das, S. Dutta, M.D.I. Bhuyan, M.N. Islam, M.A. Basith, MoS$_2$ nanosheet incorporated α-Fe$_2$O$_3$/ZnO nanocomposite with enhanced photocatalytic dye degradation and hydrogen production ability, RSC Adv. 9 (2019) 40357–40367, https://doi.org/10.1039/C9RA07526G.

[2] W. Yin, S. Hao, H. Cao, Solvothermal synthesis of magnetic CoFe$_2$O$_4$/rGO nanocomposites for highly efficient dye removal in wastewater, RSC Adv. 7 (2017) 4062–4069, https://doi.org/10.1039/C6RA26948F.

[3]   T. Torimoto, M. Tada, M. Dai, T. Kameyama, S. Suzuki, S. Kuwabata, Tunable photoelectrochemical properties of chalcopyrite $AgInS_2$ nanoparticles size-controlled with a photoetching technique, J. Phys. Chem. C 116 (2012) 21895–21902, https://doi.org/10.1021/jp307305q.

[4]   K.P. Kadlag, M.J. Rao, A. Nag, Ligand-free, colloidal, and luminescent metal sulfide nanocrystals, J. Phys. Chem. Lett. 4 (2013) 1676–1681, https://doi.org/10.1021/jz4007096.

[5]   M. Deng, S. Shen, X. Wang, Y. Zhang, H. Xu, T. Zhang, Q. Wang, Controlled synthesis of $AgInS_2$ nanocrystals and their application in organic–inorganic hybrid photodetectors, CrystEngComm 15 (2013) 6443, https://doi.org/10.1039/c3ce40173a.

[6]   D.C. Look, Recent advances in ZnO materials and devices, Mater. Sci. Eng. B 80 (2001) 383–387, https://doi.org/10.1016/S0921-5107(00)00604-8.

[7]   H. Kidowaki, T. Oku, T. Akiyama, A. Suzuki, B. Jeyadevan, J. Cuya, Fabrication and characterization of CuO-based solar cells, J. Mater. Sci. Res. 1 (2011), https://doi.org/10.5539/jmsr.v1n1p138.

[8]   R. Ben Ayed, M. Ajili, A. Thamri, N.T. Kamoun, A. Abdelghani, Substrate temperature effect on the crystal growth and optoelectronic properties of sprayed α-Fe_2O_3 thin films: application to gas sensor and novel photovoltaic solar cell structure, Mater. Technol. 33 (2018) 769–783, https://doi.org/10.1080/10667857.2018.1503385.

[9]   Q. Guo, C. Zhou, Z. Ma, X. Yang, Fundamentals of TiO_2 photocatalysis: concepts, mechanisms, and challenges, Adv. Mater. 31 (2019), 1901997, https://doi.org/10.1002/adma.201901997.

[10] L. Song, S. Zhang, B. Chen, D. Sun, Highly active NiO–CaO photocatalyst for degrading organic contaminants under visible-light irradiation, Catal. Commun. 10 (2009) 421–423, https://doi.org/10.1016/j.catcom.2008.08.032.

[11] M. Shkir, A. Khan, M. Imran, M. Ajmal Khan, R.A. Zargar, T. Alshahrani, K. Deva Arun Kumar, P. Mohanraj, K.V. Chandekar, S. AlFaify, Spray pyrolysis developed Nd doped Co_3O_4 nanostructured thin films and their structural, and opto-nonlinear properties for optoelectronics applications, Opt Laser. Technol. 150 (2022), 107959, https://doi.org/10.1016/j.optlastec.2022.107959.

[12] S. Huang, C. Chen, H. Tsai, J. Shaya, C. Lu, Photocatalytic degradation of thiobencarb by a visible light-driven MoS_2 photocatalyst, Sep. Purif. Technol. 197 (2018) 147–155, https://doi.org/10.1016/j.seppur.2018.01.009.

[13] A. Islam, S.H. Teo, M.R. Awual, Y.H. Taufiq-Yap, Improving the hydrogen production from water over MgO promoted Ni–Si/CNTs photocatalyst, J. Clean. Prod. 238 (2019), 117887, https://doi.org/10.1016/j.jclepro.2019.117887.

[14] A. Addamiano, Preparation and photoluminescence of silicon carbide phosphors doped with group IIIa elements and/or nitrogen, J. Electrochem. Soc. 113 (1966) 134, https://doi.org/10.1149/1.2423885.

[15] M.I. McMahon, R.J. Nelmes, New structural systematics in the II–VI, III–V, and group-IV semiconductors at high pressure, Phys. Status Solidi 198 (1996) 389–402, https://doi.org/10.1002/pssb.2221980151.

[16] M.S. Hossain, S. Ahmed, Synthesis of nano-crystallite gypsum and bassanite from waste Pila globosa shells: crystallographic characterization, RSC Adv. 12 (2022) 25096–25105, https://doi.org/10.1039/d2ra04881g.

[17] M. Bin Mobarak, M.S. Hossain, F. Chowdhury, S. Ahmed, Synthesis and characterization of CuO nanoparticles utilizing waste fish scale and exploitation of XRD peak profile analysis for approximating the structural parameters, Arab. J. Chem. 15 (2022), 104117, https://doi.org/10.1016/j.arabjc.2022.104117.

[18] A.K. Prajapati, M.K. Mondal, Novel green strategy for CuO–ZnO–C nanocomposites fabrication using marigold (Tagetes spp.) flower petals extract with and without CTAB treatment for adsorption of Cr(VI) and Congo red dye, J. Environ. Manag. 290 (2021), 112615, https://doi.org/10.1016/j.jenvman.2021.112615.

[19] M. Kim, J.-H. Seo, U. Singisetti, Z. Ma, Recent advances in free-standing single crystalline wide band-gap semiconductors and their applications: GaN, SiC, ZnO, β-Ga_2O_3, and diamond, J. Mater. Chem. C 5 (2017) 8338–8354, https://doi.org/10.1039/C7TC02221B.

[20] S.B. Aziz, Modifying poly(vinyl alcohol) (PVA) from insulator to small-bandgap polymer: a novel approach for organic solar cells and optoelectronic devices, J. Electron. Mater. 45 (2016) 736–745, https://doi.org/10.1007/s11664-015-4191-9.

[21] Y. Sa, Y. Guo, X. Feng, M. Wang, P. Li, Y. Gao, X. Yang, T. Jiang, Are different crystallinity-index-calculating methods of hydroxyapatite efficient and consistent? New J. Chem. 41 (2017) 5723–5731, https://doi.org/10.1039/c7nj00803a.

[22] F. Dawood, M. Anda, G.M. Shafiullah, Hydrogen production for energy: an overview, Int. J. Hydrogen Energy 45 (2020) 3847–3869, https://doi.org/10.1016/j.ijhydene.2019.12.059.

[23] S. Das, S. Dutta, A.M. Tama, M.A. Basith, Nanostructured $LaFeO_3$-MoS_2 for efficient photodegradation and photocatalytic hydrogen evolution, Mater. Sci. Eng. B 271 (2021), 115295, https://doi.org/10.1016/j.mseb.2021.115295.

[24] S.K. Sen, M.R. Munshi, A. Kumar, A.A. Mortuza, M.S. Manir, M.A. Islam, M.N. Hossain, M.K. Hossain, Structural, optical, magnetic, and enhanced antibacterial properties of hydrothermally synthesized Sm-incorporating α-MoO_3 2D-layered nanoplates, RSC Adv. 12 (2022) 34584–34600, https://doi.org/10.1039/D2RA05304G.

[25] J. Shen, S. Guo, C. Chen, L. Sun, S. Wen, Y. Chen, S. Ruan, Synthesis of Ni-doped α-MoO_3 nanolamella and their improved gas sensing properties, Sensor. Actuator. B Chem. 252 (2017) 757–763, https://doi.org/10.1016/j.snb.2017.06.040.

[26] F. Wang, C. Di Valentin, G. Pacchioni, Electronic and structural properties of WO_3: a systematic hybrid DFT study, J. Phys. Chem. C 115 (2011) 8345–8353, https://doi.org/10.1021/jp201057m.

[27] P.A. Arasu, R.V. Williams, Effect of annealing temperature on structural and optical parameters of sol–gel routed molybdenum oxide thin film, Surf. Rev. Lett. 22 (2015), 1550054, https://doi.org/10.1142/S0218625X15500547.

[28] L. Zheng, Y. Xu, D. Jin, Y. Xie, Novel metastable hexagonal MoO_3 nanobelts: synthesis, photochromic, and electrochromic properties, Chem. Mater. 21 (2009) 5681–5690, https://doi.org/10.1021/cm9023887.

[29] K. Maeda, M. Eguchi, T. Oshima, Perovskite oxide nanosheets with tunable band-edge potentials and high photocatalytic hydrogen-evolution activity, Angew. Chem. Int. Ed. 53 (2014) 13164–13168, https://doi.org/10.1002/anie.201408441.

[30] H. Yan, X. Wang, M. Yao, X. Yao, Band structure design of semiconductors for enhanced photocatalytic activity: the case of TiO_2, Prog. Nat. Sci.: Mater. Int. 23 (2013) 402–407, https://doi.org/10.1016/j.pnsc.2013.06.002.

[31] R.S. Mulliken, Electronic population analysis on LCAO–MO molecular wave functions. II. Overlap populations, bond orders, and covalent bond energies, J. Chem. Phys. 23 (1955) 1841–1846, https://doi.org/10.1063/1.1740589.

[32] D. Sanchez-Portal, E. Artacho, J.M. Soler, Projection of plane-wave calculations into atomic orbitals, Solid State Commun. 95 (1995) 685–690, https://doi.org/10.1016/0038-1098(95)00341-X.

[33] M.R. Munshi, S.K. Sen, M.Z. Rana, Electronic, thermodynamic, optical and photocatalytic properties of $GaAgO_2$ and $AlAgO_2$ compounds scrutinized via a systemic hybrid DFT, Comput. Condens. Matter. 34 (2023), e00778, https://doi.org/10.1016/j.cocom.2022.e00778.

[34] M.R. Munshi, M.Z. Rana, S.K. Sen, M.R.A. Foisal, M.H. Ali, Theoretical investigation of structural, electronic, optical and thermoelectric properties of $GaAgO_2$ based on Density Functional Theory (DFT): two approach, World J. of Adv. Res. and Rev. 13 (2022) 279–291, https://doi.org/10.30574/wjarr.2022.13.2.0130.

[35] X. Liu, J. Liu, R. Qiao, Y. Yu, H. Li, L. Suo, Y. Hu, Y.-D. Chuang, G. Shu, F. Chou, T.-C. Weng, D. Nordlund, D. Sokaras, Y.J. Wang, H. Lin, B. Barbiellini, A. Bansil, X. Song, Z. Liu, S. Yan, G. Liu, S. Qiao, T.J. Richardson, D. Prendergast, Z. Hussain, F.M.F. de Groot, W. Yang, Phase transformation and lithiation effect on electronic structure of Li_xFePO_4: an in-depth study by soft X-ray and simulations, J. of the American Chem. Soc. 134 (2012) 13708–13715, https://doi.org/10.1021/ja303225e.

[36] M.U. Salma, M. Atikur Rahman, Study of structural, elastic, electronic, mechanical, optical and thermodynamic properties of $NdPb_3$ intermetallic compound: DFT based calculations, Comput. Condens. Matter. 15 (2018) 42–47, https://doi.org/10.1016/j.cocom.2018.04.001.

[37] C. Červinka, M. Fulem, K. Růžička, Evaluation of accuracy of ideal-gas heat capacity and entropy calculations by density functional theory (DFT) for rigid molecules, J. Chem. Eng. Data 57 (2012) 227–232, https://doi.org/10.1021/je201095b.

[38] M.D.I. Bhuyan, S. Das, M.A. Basith, Sol-gel synthesized double perovskite Gd_2FeCrO_6 nanoparticles: structural, magnetic and optical properties, J. of Alloys and Compouns. 878 (2021), 160389, https://doi.org/10.1016/j.jallcom.2021.160389.

[39] J.C. Knight, J. Broeng, T.A. Birks, P.S.J. Russell, Photonic band gap guidance in optical fibers, Science 282 (1998) 1476–1478, https://doi.org/10.1126/science.282.5393.1476.

[40] J.U. Rehman, M. Usman, M.B. Tahir, A. Hussain, M. Rashid, Investigation of structural, electronics, optical, mechanical and thermodynamic properties of YRu$_2$P$_2$ compound for superconducting application, J. Supercond. Nov. Magnetism 34 (2021) 3089–3097, https://doi.org/10.1007/s10948-021-06049-9.

[41] M. Harb, D. Masih, K. Takanabe, Screened coulomb hybrid DFT investigation of band gap and optical absorption predictions of CuVO$_3$, CuNbO$_3$ and Cu$_5$Ta$_{11}$O$_{30}$ materials, Phys. Chem. Chem. Phys. 16 (2014) 18198–18204, https://doi.org/10.1039/C4CP02497D.

[42] F. Colmenero, V. Timón, Study of the structural, vibrational and thermodynamic properties of natroxalate mineral using density functional theory, J. Solid State Chem. 263 (2018) 131–140, https://doi.org/10.1016/j.jssc.2018.04.022.

[43] S.A. Sofi, D.C. Gupta, Exploration of electronic structure, mechanical stability, magnetism, and thermophysical properties of L2$_1$ structured Co$_2$XSb (X = Sc and Ti) ferromagnets, Int. J. Energy Res. 44 (2020) 2137–2149, https://doi.org/10.1002/er.5071.

[44] M.A. Islam, J. Islam, M.N. Islam, S.K. Sen, A.K.M.A. Hossain, Enhanced ductility and optoelectronic properties of environment-friendly CsGeCl$_3$ under pressure, AIP Adv. 11 (2021), 045014, https://doi.org/10.1063/5.0048849.

[45] G.-M. Rignanese, Dielectric properties of crystalline and amorphous transition metal oxides and silicates as potential high-κ candidates: the contribution of density-functional theory, J. Phys. Condens. Matter 17 (2005) R357–R379, https://doi.org/10.1088/0953-8984/17/7/R03.

[46] A.M. Ferrari, R. Orlando, M. Rérat, Ab initio calculation of the ultraviolet–visible (UV-vis) absorption spectrum, electron-loss function, and reflectivity of solids, J. Chem. Theor. Comput. 11 (2015) 3245–3258, https://doi.org/10.1021/acs.jctc.5b00199.

[47] J. Islam, A.K.M.A. Hossain, Narrowing band gap and enhanced visible-light absorption of metal-doped non-toxic CsSnCl$_3$ metal halides for potential optoelectronic applications, RSC Adv. 10 (2020) 7817–7827, https://doi.org/10.1039/C9RA10407K.

[48] S. Selvarajan, P. Malathy, A. Suganthi, M. Rajarajan, Fabrication of mesoporous BaTiO3/SnO2 nanorods with highly enhanced photocatalytic degradation of organic pollutants, J. Indus. Engin. Chem. 53 (2017) 201–212, https://doi.org/10.1016/j.jiec.2017.04.026.

[49] K. Maleh, Hassan, B.G. Kumar, S. Rajendran, J. Qin, S. Vadivel, D. Durgalakshmi, F. Gracia, M.S. Moscoso, Y. Orooji, F. Karimi, Tuning of metal oxides photocatalytic performance using Ag nanoparticles integration, J. Mol. Liq. 314 (2020), 113588, https://doi.org/10.1016/j.molliq.2020.113588.